

# A Soft-Switching Control Method for Dual Active Bridge Converter Over the Full Power and Wide Voltage Regulation Range

Yuhang ZHANG, Yong LI, Jianghu WAN, Tingkun WENG, Jie ZHANG, and Yijia CAO

**Abstract**—The dual active bridge (DAB) has been widely adopted in isolated dc-dc conversion applications due to its capability for bidirectional power transfer. Among the various control strategies for DAB converters, the triple-phase-shift (TPS) control is recognized for its effectiveness. In this article, a soft-switching control method based on TPS control is proposed, which is advantageous for enhancing the efficiency of the DAB converter over the full power and wide voltage regulation range. First, the twelve operating modes of the DAB converter are categorized. And then an innovative methodology is introduced, wherein the DAB converter is equivalently transformed into a four-switch buck-boost (FSBB) converter by decomposing the midpoint voltage waveforms on both the primary and secondary sides. On the basis of the equivalent circuit, a hybrid phase-shift control method based on the soft switching is proposed, which delineates the DAB converter into six operating modes. To secure smooth and seamless transitions between these modes, a unified uni-variate control method is presented, which is simple and readily implementable. Ultimately, a 2.5 kW prototype is constructed, and the correctness and effectiveness of the proposed method are validated via the experimental results.

**Index Terms**—Dual active bridge, equivalent circuit, full power range, soft-switching, wide voltage regulation range.

## I. INTRODUCTION

WITH the rapid development of the new energy industry, the dual active bridge (DAB) converter has been widely applied in fields such as dc micro-grids [1], energy storage systems [2], and electric vehicle onboard charging systems [3] due to its advantages of electrical isolation, high power density, bidirectional energy flow, and ease of achieving soft switching [4], [5].

---

Manuscript received December 05, 2024; revised February 06, 2025; accepted March 02, 2025. Date of publication June 30, 2025; date of current version April 18, 2025. This work was supported in part by National Nature Science Foundation of China under the Grant U22B200134, 111 Project of China under the Grant B17016, and Science and Technology Innovation Program of Hunan Province under the Grant 2023RC1038. (Corresponding author: Yong Li.)

Y. Zhang, Y. Li, T. Weng, and J. Zhang, are with the College of Electrical and Information Engineering, Hunan University, Changsha 410082, China (e-mail: yuhangzhang@hnu.edu.cn; yongli@hnu.edu.cn; vontink@hnu.edu.cn; zj0711@hnu.edu.cn).

J. Wan is with the School of Automation, Central South University, Changsha 410083, China (e-mail: wanjianghu@advancechip.com).

Y. Cao is with the School of Electrical and Information Engineering, Changsha University of Science and Technology, Changsha 410114, China (e-mail: yjcao@csust.edu.cn).

Digital Object Identifier 10.24295/CPSS TPEA.2025.00009

The DAB was originally introduced in 1991 [6]. Over time, phase-shift control has become the primary control method for the DAB [7]. Based on the number of control degrees of freedom, the control methods can be categorized into single-phase-shift (SPS) control, extended-phase-shift (EPS) control, dual-phase-shift (DPS) control, and triple-phase-shift (TPS) control [8]. There is a single phase-shift ratio between the primary and secondary bridges under SPS control, which is the simplest control method. However, during light-load conditions or if the input and output voltages are mismatched, the backflow power and current stress increase, reducing the range of soft-switching conditions [9], [10]. EPS control introduces a phase-shift ratio within the full bridge of one side, while DPS control adds the same phase-shift ratio within the bridges on both sides. Both methods reduce backflow power and current stress, extend the range of soft-switching, and enhance efficiency [11], [12]. TPS control introduces different internal phase-shift ratios within the full bridges on both sides, providing better optimization performance. However, the complexity of control is the highest under TPS control [13].

To further reduce power losses and enhance efficiency, varied solutions have been proposed. Optimized control methods aimed at suppressing backflow power are provided in [14]. A strategy for minimizing current stress is adopted in [15]. A multi-phase-shift control method based on zero-voltage switching (ZVS) is presented in [16]. Nevertheless, the aforementioned methods, which are based on EPS or DPS control, have been validated merely within a single scenario. These methods show limitations in applications with variable port voltages or transmission powers, such as in electric vehicle onboard charging systems.

Regarding achieving TPS control over a wide operating range, there are mainly two ways. One is the lookup table method, and the other is the analytical formula method. In the lookup table method, a multi-mode control method based on the boundary conditions of ZVS is discussed in [17]. However, a few switching devices still suffer hard switching in certain modes. Consequently, an approach involving frequency modulation control is proposed to expand the ZVS range. Both methods require offline computations and the use of online lookup tables. However, the discreteness of the lookup table data impact the optimization effectiveness. To address this, a method relying on artificial intelligence algorithms is given in [18], which

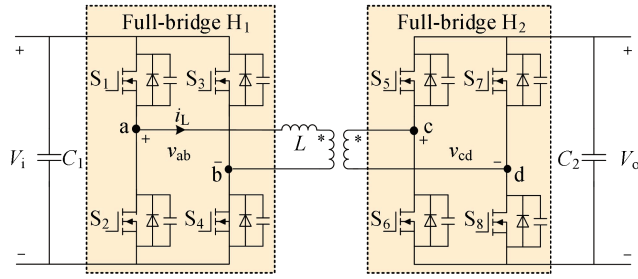


Fig. 1. Topology of the DAB converter.

improves the accuracy of the lookup table method and achieves minimum current stress. But the algorithm requires a amount of storage space, making it challenging to perform real-time calculations on general digital signal processor (DSP) controllers. In the analytical formula method, an optimized scheme that makes the converter operate with minimized root-mean-square (RMS) current across the full power range is presented in [19]. Although the efficiency has been improved under light load conditions, it remains relatively low under heavy-load conditions. A unified phase-shift control approach, aimed at minimizing current stress, is formulated in [20], using the Lagrange multiplier method (LMM). In [21], a current stress minimization control method based on full ZVS is proposed using the LMM. Nonetheless, LMM is typically employed for variable minimization at a given transmission power, posing difficulties in attaining a global optimal solution [14], [22]. The DAB converter is divided into five operating modes, within which the local optimal parameters that minimize current stress are determined in [23]. However, it does not address research on methods for mode transition. Strategies for multi-mode switching are proposed in references [24], [25]. However, the range of soft switching is limited by the voltage conversion ratio and the inductance in [24]. Although full-power-range ZVS is achieved, the efficiency significantly decreases if there is a mismatch between the input and output voltages in [25]. The analytical formula method is easier to implement compared to the lookup table method, but it still involves complex and time-consuming reasoning and calculations.

To address the limitations of existing methods, the article first analyze the division of DAB converter's operating modes under TPS control, providing the criteria and characteristics for each mode. Subsequently, the DAB converter is initially transformed into an equivalent four-switch buck-boost (FSBB) converter by decomposing the midpoint voltage waveforms of both the primary and secondary sides. By drawing parallels with the control strategies of the equivalent converter, a hybrid phase-shift control method achieving soft-switching is presented, which delineates six distinct operating modes of the DAB converter, covering the whole transferred power and a wide voltage regulation range. Furthermore, the transition processes between the modes under step-down and step-up conditions are revealed respectively. On this basis, a unified uni-variate control method is presented, which is simple to implement and achieves a smooth and seamless transition between the modes

 TABLE I  
 THE RANGE OF PHASE-SHIFT RATIOS OF EACH MODE

Mode	The value range of phase-shift ratios		
A	$A_1$	$0 \leq D_2 \leq 1,$	$D_1 \leq D_2 + D_3 - 1 \leq D_2$
	$A_2$	$1 \leq D_2 + D_3 \leq 2$	$D_2 + D_3 - 1 \leq D_1 \leq D_2$
	$A_3$		$D_2 + D_3 - 1 \leq D_2 \leq D_1$
B	$B_1$	$0 \leq D_2 \leq 1,$	$D_1 \leq D_2 \leq D_2 + D_3$
	$B_2$	$0 \leq D_2 + D_3 \leq 1$	$D_2 \leq D_1 \leq D_2 + D_3$
	$B_3$		$D_2 \leq D_2 + D_3 \leq D_1$
C	$C_1$	$-1 \leq D_2 \leq 0,$	$D_1 \leq D_2 + D_3 \leq 1 + D_2$
	$C_2$	$0 \leq D_2 + D_3 \leq 1$	$D_2 + D_3 \leq D_1 \leq 1 + D_2$
	$C_3$		$D_2 + D_3 \leq 1 + D_2 \leq D_1$
D	$D_1$	$-1 \leq D_2 \leq 0,$	$D_1 \leq 1 + D_2 \leq 1 + D_2 + D_3$
	$D_2$	$-1 \leq D_2 + D_3 \leq 0$	$1 + D_2 \leq D_1 \leq 1 + D_2 + D_3$
	$D_3$		$1 + D_2 \leq 1 + D_2 + D_3 \leq D_1$

proposed. Finally, the correctness and effectiveness of the proposed method have been verified by experiments.

The outline of this article is as follows. In Section II, the operating modes of the DAB converter are described under TPS control, and the equivalent circuit is introduced. The hybrid phase-shift control method is proposed in Section III. The unified uni-variate control method is presented in Section IV. The strategy is verified by experimental results obtained from a DAB converter prototype in Section V, followed by conclusion in Section VI.

## II. ANALYSIS OF THE EQUIVALENT CIRCUIT

### A. Topology of the DAB Converter

The topology of the DAB converter is shown in Fig. 1.  $S_1 - S_4$  form the primary full-bridge  $H_1$ , and  $S_5 - S_8$  form the secondary full-bridge  $H_2$ .  $H_1$  and  $H_2$  are connected by a high-frequency AC link, which consists of an inductor and a transformer. The voltage conversion ratio is defined as  $M = V_i / nV_o$ , and  $T_{hs}$  follows  $T_{hs} = 1/2f_s$ , where  $f_s$  is the switching frequency.

$D_1$  represents the phase-shift ratio between  $S_1$  and  $S_4$ .  $D_2$  denotes the phase-shift ratio between  $S_1$  and  $S_5$ .  $D_3$  represents the phase-shift ratio between  $S_5$  and  $S_8$ . The value ranges of the phase-shift ratios are as follows:  $0 \leq D_1 \leq 1$ ,  $-1 \leq D_2 \leq 1$ ,  $0 \leq D_3 \leq 1$ . The operating modes under TPS control are categorized into four classes (i.e., A, B, C, D) as shown in Table I, based on the variation of  $D_2$  from 1 to -1. Within each class, the modes are further divided into three sub-types based on the relative positions of the rising and falling edges of the primary and secondary side midpoint voltage waveforms. This positional relationship within half a period can be reflected through the relationships among the values of  $D_1$ ,  $(D_2 + D_3)$ , and  $D_2$ . The midpoint voltage waveforms of these modes are depicted in Fig. 2.

It can be observed in Fig. 2 that there are no regions where the primary and secondary midpoint voltages overlap in phase in modes  $A_1, A_2, A_3, C_3, D_2$ , and  $D_3$ . The peak value of the in-

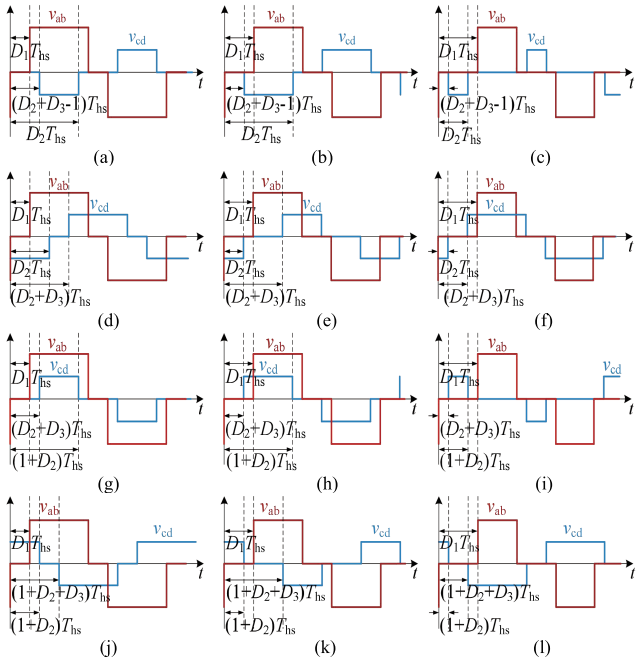


Fig. 2. Midpoint voltage waveforms of each mode under TPS control. (a) Mode A<sub>1</sub>. (b) Mode A<sub>2</sub>. (c) Mode A<sub>3</sub>. (d) Mode B<sub>1</sub>. (e) Mode B<sub>2</sub>. (f) Mode B<sub>3</sub>. (g) Mode C<sub>1</sub>. (h) Mode C<sub>2</sub>. (i) Mode C<sub>3</sub>. (j) Mode D<sub>1</sub>. (k) Mode D<sub>2</sub>. (l) Mode D<sub>3</sub>.

ductor current is higher in these six modes compared to others, resulting in increased conduction losses and reduced efficiency [26]. Besides, conditions involving reverse power, as illustrated by modes C<sub>1</sub>, C<sub>2</sub>, and D<sub>1</sub>, are not discussed. Consequently, modes B<sub>1</sub>, B<sub>2</sub>, and B<sub>3</sub> emerge as superior choices for enhancing operational efficiency of the DAB converter. Specifically, mode B<sub>1</sub> offers a transferred power range of [0, 1], enabling operation across the full power range. Mode B<sub>2</sub> has a transferred power range of [0, 2/3], while mode B<sub>3</sub> provides a transferred power range of [0, 1/2] [10].

### B. The Equivalent Circuit of the DAB Converter

Owing to the relatively complex structure of DAB converter and its complicated control methods, the paper explores the equivalent circuit of the DAB converter from the perspective of circuit structure simplification. Moreover, a control method applicable for the DAB converter is proposed based on the equivalent circuit.

Based on the principle of voltage superposition, the waveform of the primary side midpoint voltage  $v_{ab}$  of DAB converter can be decomposed into  $v_a$  and  $v_b$ , and the decomposed voltage waveforms can be equivalently generated by half-bridge circuits.

As shown in Fig. 3(a), the waveform of  $v_{ab}$  within one period is divided into states I and II. In state I, when  $v_{ab}$  is high, it can be decomposed into a high voltage  $v_a$  and a zero voltage  $v_b$ , which is the same as the voltage of points a and b when Q<sub>1</sub> is turned on and Q<sub>2</sub> is off in half-bridge A. When  $v_{ab}$  is at zero, it can be decomposed into zero voltages for both  $v_a$  and  $v_b$ , which is the same as the voltage at points a and b when Q<sub>1</sub> is off and Q<sub>2</sub> is on in half-bridge A. In state II, when  $v_{ab}$  is negative, it can be

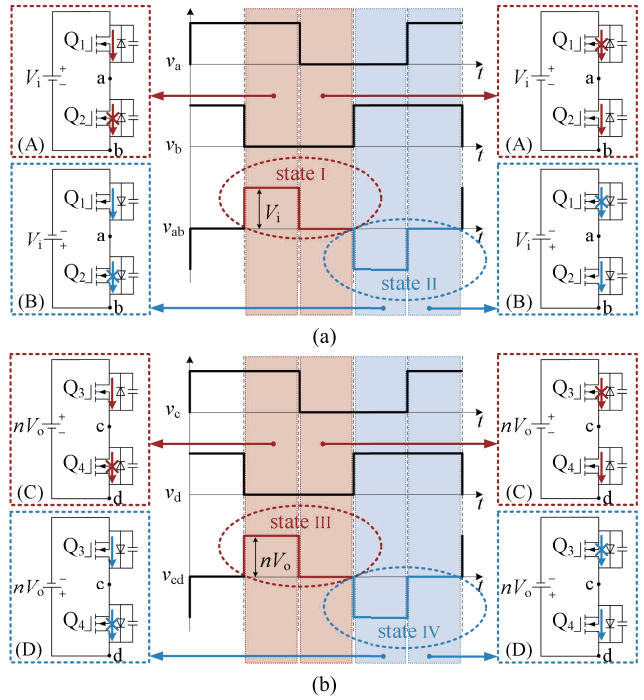


Fig. 3. Midpoint voltage waveforms and equivalent half-bridge circuits. (a) Primary side. (b) Secondary side.

decomposed into a zero voltage  $v_a$  and a high voltage  $v_b$ , which is the same as the voltage at points a and b when Q<sub>1</sub> is on and Q<sub>2</sub> is off in half-bridge B. When  $v_{ab}$  is at zero, it can be divided into high voltages for both  $v_a$  and  $v_b$ , which is the same as the voltage at points a and b when Q<sub>1</sub> is off and Q<sub>2</sub> is on in half-bridge B. Thus, state I can be equivalently generated by half-bridge A, and state II can be equivalently generated by half-bridge B.

Similarly, the waveform of the secondary side midpoint voltage  $v_{cd}$  within one cycle can be decomposed into states III and IV, as illustrated in Fig. 3(b). The waveform of state III can be equivalently generated by half-bridge C, and the waveform of state IV can be equivalently generated by half-bridge D.

On this basis, an equivalent circuit model of DAB converter can be constructed to simplify its structure.

According to the previous analysis, the classification of the operating modes of DAB converter under phase-shift control can be determined by the relative positions of the rising and falling edges of the waveforms for  $v_{ab}$  and  $v_{cd}$ . In other words, this relative positioning can be reflected through the arbitrary combination of the waveforms for  $v_{ab}$  and  $v_{cd}$ .

Within the positive half-cycle of  $v_{ab}$ , there exist two possible combinations of  $v_{ab}$  and  $v_{cd}$ , namely “state I + state III” and “state I + state IV”, as shown in their equivalent circuits in Fig. 4. According to the previous analysis, the combination of “state I + state IV” should be avoided as it lacks any coincident in phase voltage overlap, which results in decreased efficiency. Thus, the circuit of the combination “state I + state III” is selected as the equivalent circuit for DAB converter.

The equivalent circuit illustrated in Fig. 4(a) actually represents the FSBB. A multi-mode ZVS control approach is proposed

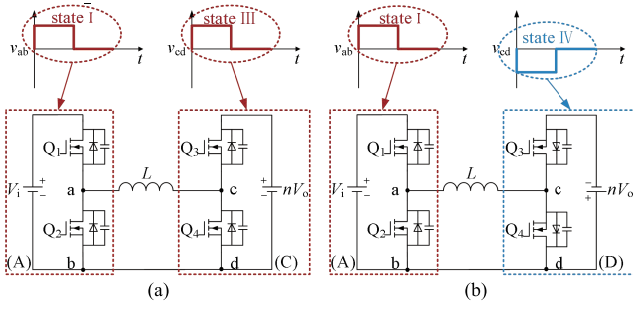


Fig. 4. Equivalent circuits of DAB converter. (a) "State I + state III". (b) "State I + state IV".

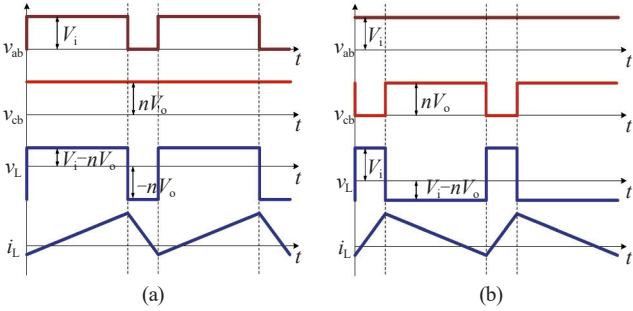


Fig. 5. Waveforms of FSBB. (a) Buck mode. (b) Boost mode.

for this converter in [27]. It indicates that the current stress is lower in both buck and boost modes compared to the Buck-Boost mode. Consequently, conduction losses are lower and operational efficiency is higher. The waveforms for the buck and boost modes are depicted in Fig. 5.

Therefore, the control method of the DAB converter can be optimized based on the buck and boost modes of the FSBB.

### III. HYBRID PHASE-SHIFT CONTROL METHOD

The condition for achieving ZVS is that the current flows through the anti-parallel diodes of the switching device before the gate signal goes high, and the condition for achieving ZCS is that the current flowing through the switching device is zero if the gate signal goes high. The soft-switching conditions of the DAB converter are listed in Table II.

#### A. The Analysis of Step-Down Condition ( $M > 1$ )

The analysis for the step-down condition is grounded in the buck mode of the FSBB. As is shown in Fig. 6(b),  $S_5$  and  $S_8$  remain on during  $t_0 - t_2$ .  $S_4$  is turned on at  $t_0$ , and the energy is directly transferred from the input side to the output side, with the inductor current increasing.  $S_1$  is turned off and  $S_2$  is on at  $t_1$ , allowing the energy stored in the inductor to continue being delivered to the output side, resulting in a decrease in current. The difference from the FSBB lies that in the latter, the current drops below zero at  $t_2$ , which allows the anti-parallel diode of  $Q_1$  to conduct, enabling ZVS for  $Q_1$  and transitioning to the next cycle. In contrast, the full-bridge structure of the

TABLE II  
SOFT-SWITCHING CONDITIONS OF THE DAB CONVERTER

Switching devices	ZVS condition	ZCS condition
$S_1, S_4, S_6, S_7$	$i_L(t) < 0$	$i_L(t) = 0$
$S_2, S_3, S_5, S_8$	$i_L(t) > 0$	$i_L(t) = 0$

DAB converter doubles the period. The negative current at  $t_2$  is unable to achieve soft-switching for  $S_3$ . Considering this,  $S_3$  should be turned on if the current drops to zero to realize ZCS. Since the transition to the next half-cycle occurs exactly at the zero-crossing point of the current, this mode is termed the buck boundary conduction mode (Buck\_BCM). The analysis for the latter half-cycle is similar to the preceding text.

As can be seen from Fig. 6(b), the ZVS conditions listed in Table II are met by the current during the conduction of  $S_1$  and  $S_2$ , and the ZCS conditions are met by the current during the conduction of  $S_3$ - $S_8$ . Therefore,  $S_1$  and  $S_2$  achieve ZVS, while  $S_3$ - $S_8$  achieve ZCS in the Buck\_BCM. The expression of the phase-shift ratios can be further derived as follows

$$\begin{cases} D_1 = D_2 + D_3 \\ D_3 = 0 \\ \frac{(V_i - nV_o)(1 - D_1)T_{hs}}{L} - \frac{nV_o D_2 T_{hs}}{L} = 0 \end{cases} \quad (1)$$

Buck\_BCM cannot meet the needs of global power operation with the fixed inductance and switching frequency of the DAB converter. Therefore, it is necessary to adjust the transferred power on the basis of Buck\_BCM by altering the magnitude or duration of the voltage across the inductor.

If the converter operates under light-load conditions, the reduction in the duration of the inductor voltage can result in discontinuous current, consequently diminishing the power delivery. This mode is defined as the buck discontinuous conduction mode (Buck\_DCM), with the operational waveform depicted in Fig. 6(a).

As observed in Fig. 6, it is evident that the current state of the switches at the moment of conduction in the Buck\_DCM is consistent with that of the Buck\_BCM. Hence,  $S_1$  and  $S_2$  achieve ZVS, and  $S_3$ - $S_8$  achieve ZCS in the Buck\_DCM. The expression of the phase-shift ratios can be derived as follows

$$\begin{cases} D_1 = D_2 + D_3 \\ \frac{(V_i - nV_o)(1 - D_1)T_{hs}}{L} - \frac{nV_o D_2 T_{hs}}{L} = 0 \end{cases} \quad (2)$$

Under heavy-load conditions, the transferred power can be enhanced by increasing the inductor voltage, which leads to a rapid increase in current. There are two methods to increase the inductor voltage. One method involves increasing the voltage to  $V_i + nV_o$ , and its operational waveforms is illustrated in red in Fig. 7, with the red shaded area representing the transferred

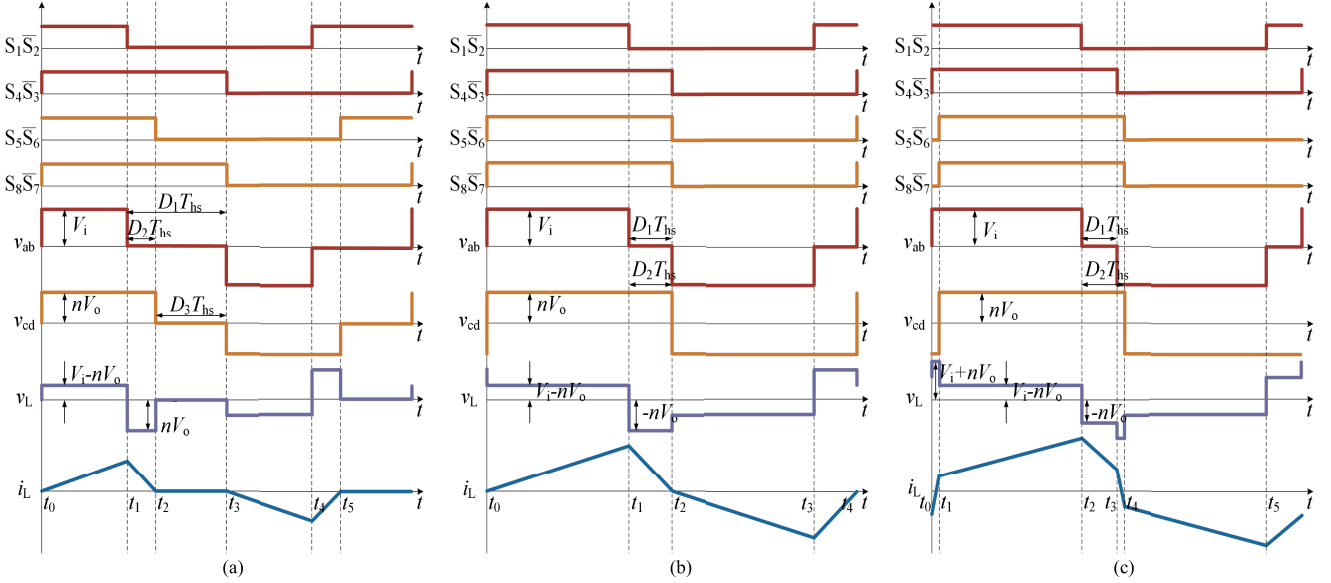


Fig. 6. Operational waveforms of the DAB converter under step-down condition. (a) Buck\_DCM. (b) Buck\_BCM. (c) Buck\_CCM.

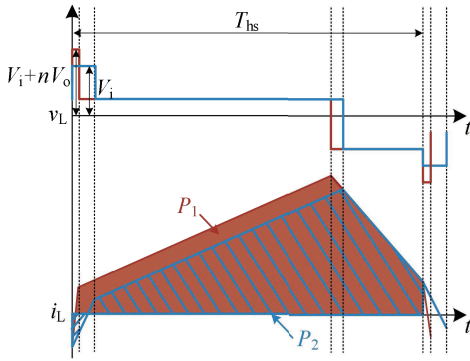


Fig. 7. Comparison of operational waveforms in two methods.

power  $P_1$ . The other method involves increasing the voltage to  $V_i$ , and its operational waveforms is depicted in blue in Fig. 7, with the blue shaded area representing the transferred power  $P_2$ .

Based on the inductor voltage and current waveforms shown in Fig. 7, the expression for the transferred power can be derived as follows

$$P = V_i \cdot \frac{1}{T_{hs}} \int_0^{T_{hs}} i_L(t) dt \quad (3)$$

Taking the maximum power  $P_b$  of SPS control as [28], the p.u. value of  $P_1$  is

$$\begin{aligned} P_1 &= V_i \cdot \frac{1}{P_b T_{hs}} \int_0^{T_{hs}} i_L(t) dt \\ &= \frac{(-MD_1 + 2MD_2 - M + 1)^2}{2(M+1)} - \frac{(MD_1 + 2D_1 - 2D_2 - M + 1)^2}{2(M+1)} + \\ &\quad 2(-MD_1 + MD_2 + D_2)(1 - D_2) + 2D_1(-MD_1 - D_1 + 2D_2 + M - 1) \end{aligned} \quad (4)$$

Similarly, the p. u. value of  $P_2$  is

$$\begin{aligned} P_2 &= V_i \cdot \frac{1}{P_b T_{hs}} \int_0^{T_{hs}} i_L(t) dt \\ &= \frac{(-MD_1 + D_1 + 2MD_2 - D_2 - M + 1)^2}{2M} - \\ &\quad \frac{(-MD_1 - D_1 + D_2 + M - 1)^2}{2M} + 2(-MD_1 + D_1 + MD_2)(1 - D_2) + \\ &\quad 2D_1(-MD_1 + D_2 + M - 1) \end{aligned} \quad (5)$$

In addition,  $D_1$  and  $D_2$  satisfy the following constraint condition within these two methods:

$$D_1 < D_2 \quad (6)$$

According to (4) – (6), the relationship between the transferred power and the phase shift ratios is plotted for different values of  $M$ , as shown in Fig. 8. It can be observed that  $P_1$  is always greater than  $P_2$  under the constraint condition. Thus, elevating the inductor voltage to  $V_i + nV_o$  is the optimal choice for enhancing the transferred power under heavy load conditions.

Since the inductor current remains continuously conductive, this mode is defined as the buck continuous conduction mode (Buck\_CCM), with its operational waveform presented in Fig. 6(c).

It can be observed in Fig. 6(c) that ZVS conditions indicated in Table II are satisfied by the current of each switch at the moment of conduction. Therefore,  $S_1$ – $S_8$  all achieve ZVS in the Buck\_CCM. The expression of the phase-shift ratios can be further derived as follows

$$D_3 = 0 \quad (7)$$

### B. The Analysis of Step-Up Condition ( $M < 1$ )

The analysis for the step-up operation is based on the boost mode of the FSBB. As is shown in Fig. 9(b),  $S_1$  and  $S_4$  are conductive during  $t_0 - t_2$ .  $S_5$  is turned on at  $t_0$ , and energy from

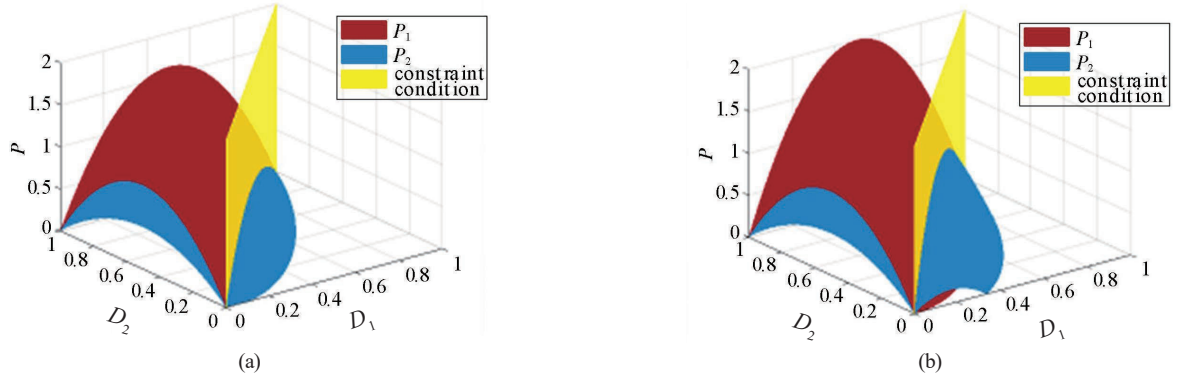
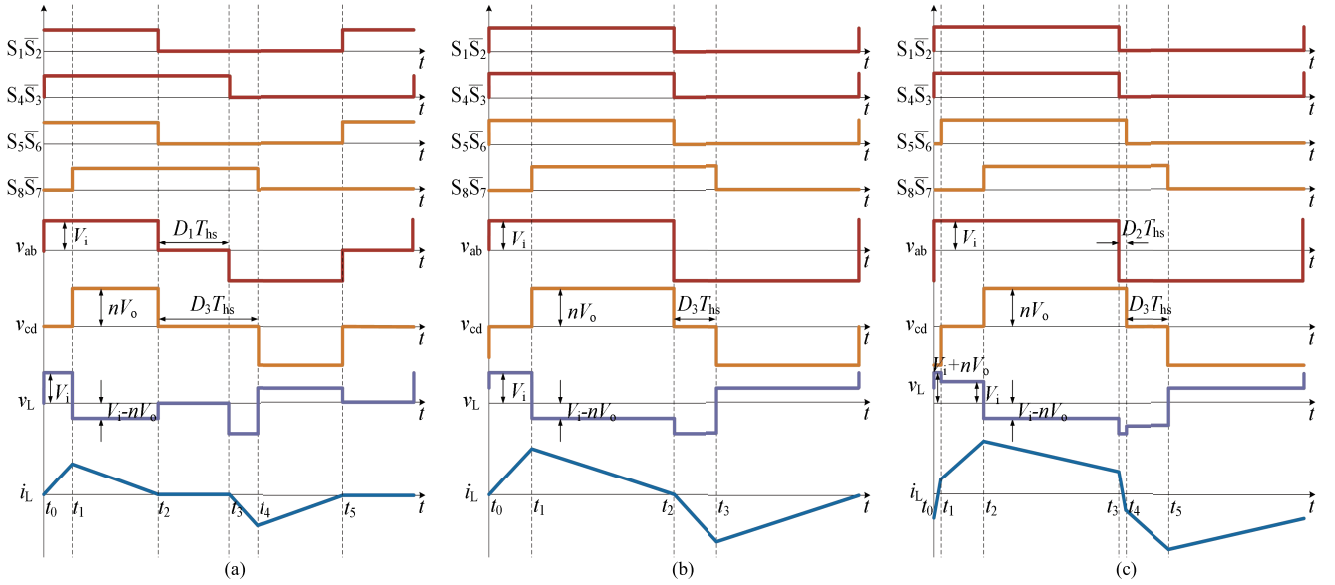

 Fig. 8. Comparison of transferred power between two methods. (a)  $M=1.2$ . (b)  $M=2$ .


Fig. 9. Operational waveforms of the DAB converter under step-up condition. (a) Boost\_DCM. (b) Boost\_BCM. (c) Boost\_CCM.

the input side is stored in the inductor, with the inductor current increasing.  $S_7$  is turned off and  $S_8$  is on at  $t_1$ , causing both the input side and the inductor to transfer energy to the output side, resulting in a decrease in current. The current decreases to zero at  $t_2$ , at which point  $S_6$  is turned on with ZCS. Similar to the Buck\_BCM, this mode is defined as the boost boundary conduction mode (Boost\_BCM).

From Fig. 9(b), it can be seen that the ZVS conditions specified in Table II are met by the current of  $S_7$  and  $S_8$  at the moment of conduction, and the ZCS conditions are met by the current of  $S_1$ – $S_6$  at the moment of conduction. As a result,  $S_7$  and  $S_8$  achieve ZVS, and  $S_1$ – $S_6$  achieve ZCS in the Boost\_BCM. The expression of the phase-shift ratios can be further derived as follows

$$\begin{cases} D_1 = D_2 = 0 \\ \frac{V_i D_3 T_{hs}}{L} - \frac{(V_i - nV_o)(T_{hs} - D_3 T_{hs})}{L} = 0 \end{cases} \quad (8)$$

Under light-load conditions, reducing the duration of the inductor voltage leads to decreased transferred power. This

mode is defined as the boost discontinuous conduction mode (Boost\_DCM), and its waveform is shown in Fig. 9(a).

In Fig. 9, the current state of the switches at the moment of conduction in Boost\_DCM is identical to that of Boost\_BCM. Consequently,  $S_7$  and  $S_8$  achieve ZVS, and  $S_1$ – $S_6$  achieve ZCS in Boost\_DCM. The expression of the phase-shift ratios can be further derived as follows

$$\begin{cases} D_2 = 0 \\ \frac{V_i (D_3 - D_1) T_{hs}}{L} - \frac{(V_i - nV_o)(T_{hs} - D_3 T_{hs})}{L} = 0 \end{cases} \quad (9)$$

Under heavy-load operations, the power transferred can be enhanced by raising the inductor voltage to  $V_i + nV_o$ . This mode is defined as the boost continuous conduction mode (Boost\_CCM) because the current remains continuous, with the waveform illustrated in Fig. 9(c).

In Fig. 9(c), ZVS conditions outlined in Table II are satisfied by the current of all switches at the moment of conduction. Therefore,  $S_1$ – $S_8$  all achieve ZVS in the Boost\_CCM. The expression of the phase-shift ratios can be further derived as follows

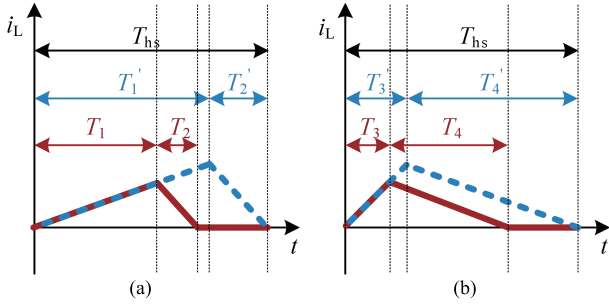


Fig. 10. Inductor current waveforms under DCM and BCM. (a) Buck\_DCM and Buck\_BCM. (b) Boost\_DCM and Boost\_BCM.

$$D_1 = 0 \quad (10)$$

This method is termed the hybrid phase-shift control method due to its implementation of multi-mode and multi-phase-shift control.

Regarding the power transmission capability, the six operating modes can be categorized according to the relationships of the phase shift ratios. Buck\_CCM and Boost\_CCM are grouped under mode B<sub>1</sub>, shown in Table I. As analyzed in Section II, this mode covers the entire range of transferred power, enabling the DAB converter to operate under heavy load conditions. Boost\_DCM and Boost\_BCM are classified as mode B<sub>2</sub>, and Buck\_DCM and Buck\_BCM are classified as mode B<sub>3</sub>, with their respective transferred power ranges being [0, 2/3] and [0, 1/2]. These two modes are suitable for the DAB converter to operate under light and medium load conditions.

#### IV. A UNIFIED UNI-VARIATE CONTROL METHOD

To meet diverse transferred power requirements, three operating modes are proposed in the previous section for both step-down and step-up conditions. However, the transferred power is not static, and DAB converter is required to transit seamlessly among the various modes in practical applications. Therefore, a unified uni-variate control method which is simple and feasible is proposed in this section to meet the need of transitions.

##### A. Transition Method for Discontinuous Conduction of Current

The waveforms of DCM and BCM under both step-down and step-up conditions are illustrated in Fig. 10. The solid red lines represent DCM, and the dashed blue lines represent BCM.

In the Buck\_DCM, the inductor current initially rises with a slope of  $(V_i - nV_o)/L$  over a period  $T_1$ , then falls with a slope of  $nV_o/L$  over a period  $T_2$ . In the Buck\_BCM, the inductor current first increases with a slope of  $(V_i - nV_o)/L$  over a period  $T_1'$ , and then decreases with a slope of  $nV_o/L$  over a period  $T_2'$ . These two periods satisfy the following expression

$$T_1' + T_2' = T_{hs} \quad (11)$$

It can be observed that as the transferred power increases,  $T_1$  gradually increases to  $T_1'$ ,  $T_2$  increases to  $T_2'$ . The periods all satisfy the following expression

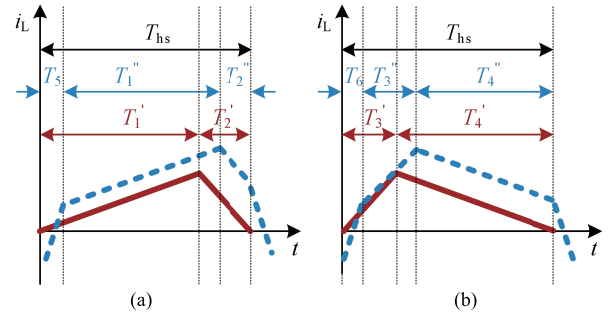


Fig. 11. Inductor current waveforms under BCM and CCM. (a) Buck\_BCM and Buck\_CCM. (b) Boost\_BCM and Boost\_CCM.

$$\frac{T_1'}{T_2'} = \frac{T_1}{T_2} = \frac{nV_o}{V_i - nV_o} \quad (12)$$

By solving (11) and (12),  $T_1'$  and  $T_2'$  can be expressed as

$$\begin{cases} T_1' = \frac{nV_o}{V_i} \cdot T_{hs} \\ T_2' = \frac{V_i - nV_o}{V_i} \cdot T_{hs} \end{cases} \quad (13)$$

It is evident that  $T_1$  and  $T_2$  are coupled in (12). Therefore, during the transition from Buck\_DCM to Buck\_BCM,  $T_2$  will be automatically regulated if  $T_1$  is adjusted.

In Boost\_DCM, the inductor current first rises with a slope of  $V_i/L$  over a time period  $T_3$ , then falls with a slope of  $(V_i - nV_o)/L$  over a time period  $T_4$ . In the Boost\_BCM, the inductor current first increases with a slope of  $V_i/L$  over a time period  $T_3'$ , then decreases with a slope of  $(V_i - nV_o)/L$  over a time period  $T_4'$ . These two periods satisfy the following expression

$$T_3' + T_4' = T_{hs} \quad (14)$$

It can be seen that  $T_3$  gradually increases to  $T_3'$ ,  $T_4$  gradually increases to  $T_4'$  with the transferred power increasing. The periods all satisfy the following expression

$$\frac{T_3'}{T_4'} = \frac{T_3}{T_4} = \frac{nV_o - V_i}{V_i} \quad (15)$$

By solving (14) and (15),  $T_3'$  and  $T_4'$  can be expressed as

$$\begin{cases} T_3' = \frac{nV_o - V_i}{nV_o} \cdot T_{hs} \\ T_4' = \frac{V_i}{nV_o} \cdot T_{hs} \end{cases} \quad (16)$$

It is apparent that  $T_3$  and  $T_4$  are also coupled in (15). Therefore, the transition from Boost\_DCM to Boost\_BCM can be achieved by adjusting  $T_3$ , and  $T_4$  is regulated accordingly.

##### B. Transition Method for Continuous Conduction of Current

Fig. 11 gives the waveforms of BCM and CCM under both step-down and step-up conditions, with solid red lines repre-

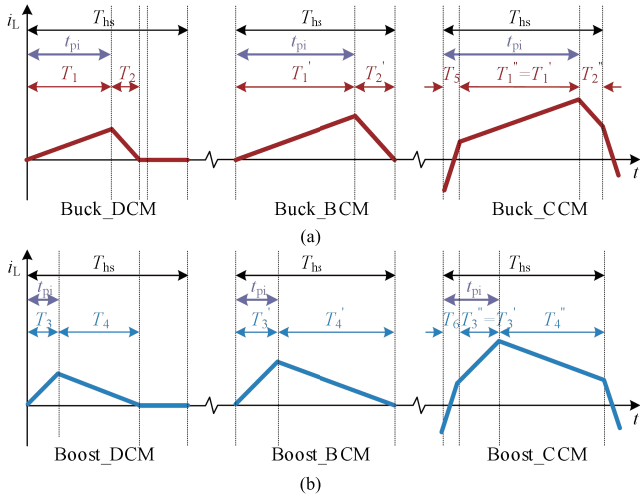


Fig. 12. The transitions among DCM, BCM and CCM. (a) Step-down condition. (b) Step-up condition.

senting BCM and dashed blue lines representing CCM.

In the Buck\_CCM waveform shown in Fig. 11(a), the inductor current initially rises with a slope of  $(V_i + nV_o)/L$  over a period  $T_5$ , then continues to rise with a slope of  $(V_i - nV_o)/L$  over a period  $T_1''$ , and finally falls with a slope of  $nV_o/L$  over a period  $T_2''$ . These periods satisfy the following expression

$$T_1'' + T_2'' + T_5 = T_{hs} \quad (17)$$

Based on the analysis in subsection A of Section III, in the shift from Buck\_BCM to Buck\_CCM, it is optimal to increase the inductor voltage to  $V_i + nV_o$ , thereby introducing  $T_5$ . When the transferred power needs to be adjusted in Buck\_CCM, there are three control degrees of freedom (i.e.,  $T_5$ ,  $T_1''$ ,  $T_2''$ ), which increase the complexity of control. Thus, it is advisable to keep  $T_1''$  equal to  $T_1'$ . When adjusting  $T_5$ ,  $T_2''$  will be automatically adjusted according to (17).

In Boost\_CCM waveform shown in Fig. 11(b), the inductor current first rises with a slope of  $(V_i + nV_o)/L$  over a period  $T_6$ , then increases with a slope of  $V_i/L$  over a period  $T_3''$ , and subsequently decreases with a slope of  $(nV_o - V_i)/L$  over a period  $T_4''$ . These periods satisfy the following expression

$$T_3'' + T_4'' + T_6 = T_{hs} \quad (18)$$

During the transition from Boost\_BCM to Boost\_CCM, raising the inductor voltage to  $V_i + nV_o$ , which introduces  $T_6$ . In Boost\_CCM, by keeping  $T_3''$  equal to  $T_3'$ , the transferred power can be adjusted by varying  $T_6$ , with  $T_4''$  automatically adjusting in accordance with (18).

### C. The Principle of the Unified Uni-Variate Control Method

Fig. 12 illustrates the transitions among DCM, BCM and CCM. Based on the analysis from the previous subsections, the transitions can be achieved by adjusting  $T_1$  and  $T_5$  under step-down conditions. To reduce the complexity of control, a unified control variable  $t_{pi}$  is defined to regulate  $T_1$  and  $T_5$  in Fig. 12(a).

In Buck\_DCM, the value of  $t_{pi}$  ranges from  $[0, T_1]$ , and the

expression of  $t_{pi}$  is

$$t_{pi} = T_1 \quad (19)$$

Furthermore, the expressions for the phase-shift ratios can be calculated as follows in conjunction with (2)

$$\begin{cases} D_1 = 1 - \frac{t_{pi}}{T_{hs}} \\ D_2 = \frac{V_i - nV_o}{nV_o} \cdot \frac{t_{pi}}{T_{hs}} \\ D_3 = 1 - \frac{V_i}{nV_o} \cdot \frac{t_{pi}}{T_{hs}} \end{cases} \quad (20)$$

In Buck\_BCM, the expression of  $t_{pi}$  is

$$t_{pi} = T_1' = \frac{nV_o}{V_i} \cdot T_{hs} \quad (21)$$

At this time, the phase-shift ratios still satisfy (20).

In Buck\_CCM, the range of  $t_{pi}$  is  $[T_1', T_{hs}]$ , and the expression of  $t_{pi}$  is

$$t_{pi} = T_5 + T_1'' = T_5 + \frac{nV_o}{V_i} \cdot T_{hs} \quad (22)$$

By integrating (7), the expressions for the phase-shift ratios can be derived as follows

$$\begin{cases} D_1 = 1 - \frac{t_{pi}}{T_{hs}} \\ D_2 = 1 - \frac{nV_o}{V_i} \\ D_3 = 0 \end{cases} \quad (23)$$

As the transferred power increases, the value of  $t_{pi}$  will monotonically increase according to (19), (21) and (22). Since  $t_{pi}$  changes continuously, the transition process between modes is also continuous and smooth.

Under step-up conditions, the transitions can be realized by controlling  $T_3$  and  $T_6$ . Similarly to the step-down conditions,  $t_{pi}$  can still be used to regulate  $T_3$  and  $T_6$  in Fig. 12(b).

In Boost\_DCM, the value of  $t_{pi}$  ranges from  $[0, T_3]$ , and the expression of  $t_{pi}$  is

$$t_{pi} = T_3 \quad (24)$$

The expressions for the phase-shift ratios can be calculated by combining (9) as follows

$$\begin{cases} D_1 = 1 - \frac{nV_o}{nV_o - V_i} \cdot \frac{t_{pi}}{T_{hs}} \\ D_2 = 0 \\ D_3 = 1 - \frac{V_i}{nV_o - V_i} \cdot \frac{t_{pi}}{T_{hs}} \end{cases} \quad (25)$$

In Boost\_BCM, the expression of  $t_{pi}$  is

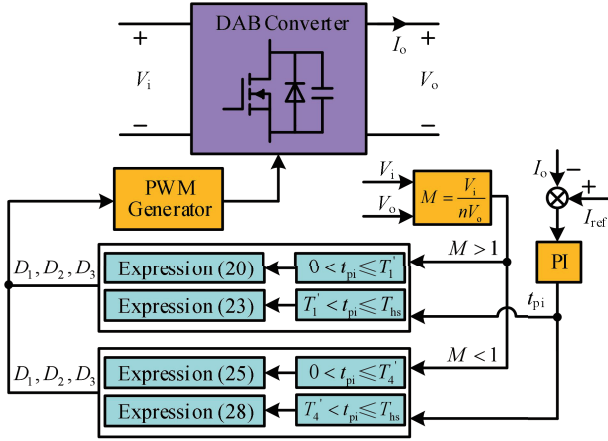


Fig. 13. The closed-loop control system of the unified uni-variate control method.

$$t_{pi} = T_3' = \frac{nV_o - V_i}{nV_o} \cdot T_{hs} \quad (26)$$

At this point, the phase-shift ratios still satisfy (25).

In Boost\_CCM, the range of  $t_{pi}$  is  $[T_3', T_{hs}]$ , and its expression is given by

$$t_{pi} = T_6 + T_3'' = T_6 + \frac{nV_o - V_i}{nV_o} \cdot T_{hs} \quad (27)$$

Furthermore, the expressions for the phase-shift ratios can be derived as follows in conjunction with (10)

$$\begin{cases} D_1 = 0 \\ D_2 = \frac{t_{pi}}{T_{hs}} - \frac{nV_o - V_i}{nV_o} \\ D_3 = \frac{nV_o - V_i}{nV_o} \end{cases} \quad (28)$$

Drawing from (24), (26) and (27), it is evident that the value of  $t_{pi}$  increases steadily and monotonically with the transferred power increasing, thereby achieving a smooth transition between modes.

As shown in Fig. 13, the closed-loop control system of the unified uni-variate control method is constructed. First, the input voltage  $V_i$  and output voltage  $V_o$  of the DAB converter are sampled to calculate the voltage conversion ratio  $M$ , which determines whether the converter is operating under step-down conditions or step-up conditions. Meanwhile, the output current  $I_o$  is sampled, and the difference between the reference current  $I_{ref}$  and  $I_o$  is fed into a PI controller. The output of the PI controller serves as the unified control variable  $t_{pi}$ . Subsequently,  $V_i$ ,  $V_o$  and  $t_{pi}$  are input into the computational model to determine the phase-shift ratios  $D_1$ ,  $D_2$  and  $D_3$ . Finally, the phase-shift ratios are entered into the PWM generator to produce the driving signals, which control the switches of the DAB converter. It is evident that the three phase-shift ratios  $D_1$ ,  $D_2$  and  $D_3$  can be managed by merely adjusting the value of  $t_{pi}$ , thereby reducing the complexity of control. In addition, only four expressions are necessary for the computational model, making the modulation scheme to be readily implemented us-

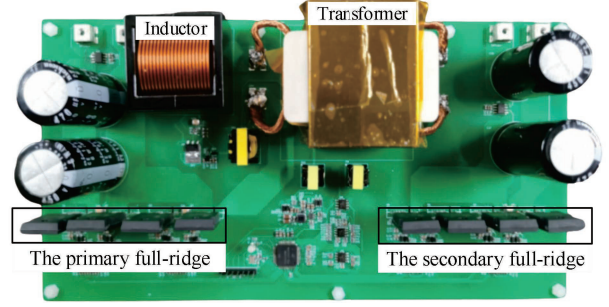
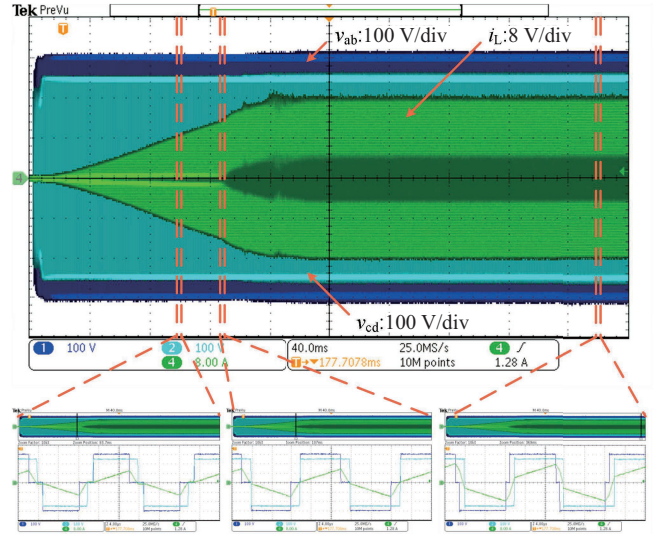


Fig. 14. The 2.5 kW prototype of the DAB converter.

TABLE III  
EXPERIMENTAL PARAMETERS

Parameter	Value
Input dc voltage	300 V
Output dc voltage	230–370 V
Inductance	30 $\mu$ H
Transformer turn ratio	1 : 1
Switching frequency	50 kHz

Fig. 15. The waveform over full power range with  $V_i = 300$  V,  $V_o = 250$  V.

ing general DSP.

## V. EXPERIMENTAL VERIFICATION

As shown in Fig. 14, a 2.5 kW prototype of DAB converter is built by SiC MOSFET (i.e., GC3M0040120K) in the laboratory. The control algorithms are implemented by the DSP (i.e., TMS320F280049), and the experimental parameters are listed in Table III. In order to verify the effectiveness of the proposed method under various values of  $M$ , experiments are conducted by setting  $V_o$  to different values.

### A. The Experiment Under Step-Down Conditions ( $M > 1$ )

An experiment is conducted with the settings  $V_i = 300$  V,  $V_o = 250$  V. It can be seen from Fig. 15 that as the transferred

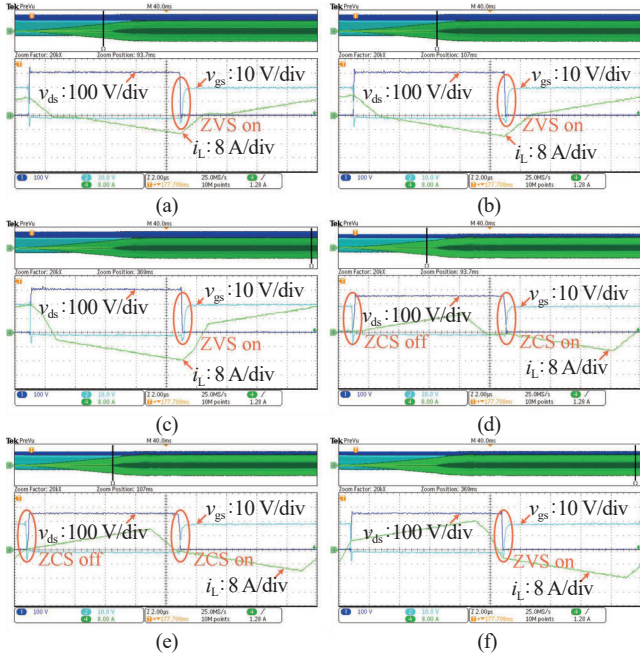


Fig. 16. The switching waveforms with  $V_i = 300$  V,  $V_o = 250$  V. (a)  $S_1$  in Buck\_DCM. (b)  $S_1$  in Buck\_BCM. (c)  $S_1$  in Buck\_CCM. (d)  $S_7$  in Buck\_DCM. (e)  $S_7$  in Buck\_BCM. (f)  $S_7$  in Buck\_CCM.

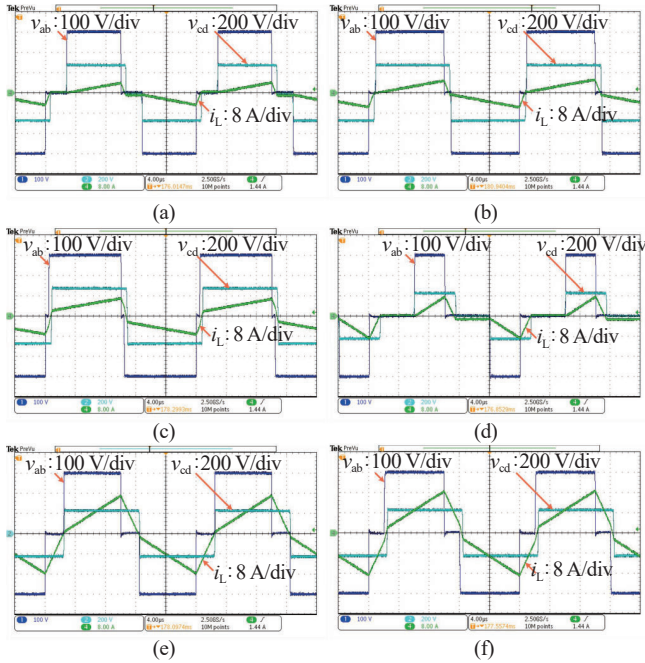


Fig. 17. The waveforms under step-down conditions with  $V_i = 300$  V. (a)  $V_o = 280$  V in Buck\_DCM. (b)  $V_o = 280$  V in Buck\_BCM. (c)  $V_o = 280$  V in Buck\_CCM. (d)  $V_o = 230$  V in Buck\_DCM. (e)  $V_o = 230$  V, in Buck\_BCM. (f)  $V_o = 230$  V in Buck\_CCM.

power increases, the converter sequentially operates in Buck\_DCM, Buck\_BCM, and Buck\_CCM, achieving smooth transitions. The switching waveforms of  $S_1$  and  $S_7$  are displayed in Fig. 16. Across all three modes,  $S_1$  consistently achieves ZVS, and  $S_2$  exhibits similar behavior.  $S_7$  achieves ZCS in Buck\_DCM and Buck\_BCM, and ZVS in Buck\_CCM.  $S_3 - S_6$  and

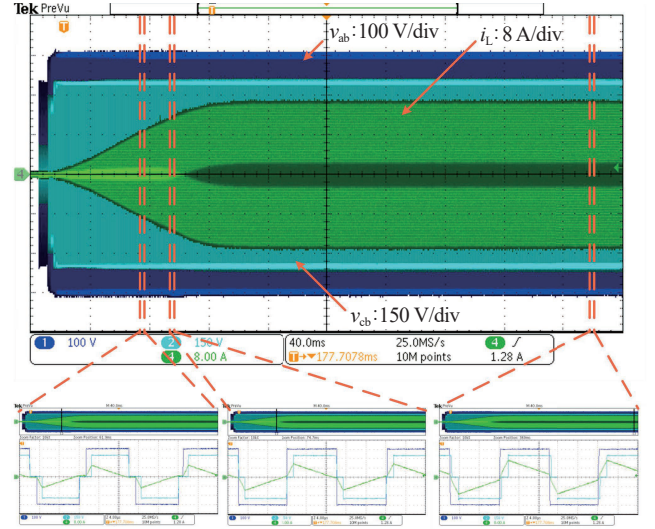


Fig. 18. The waveform over full power range with  $V_i = 300$  V,  $V_o = 350$  V.

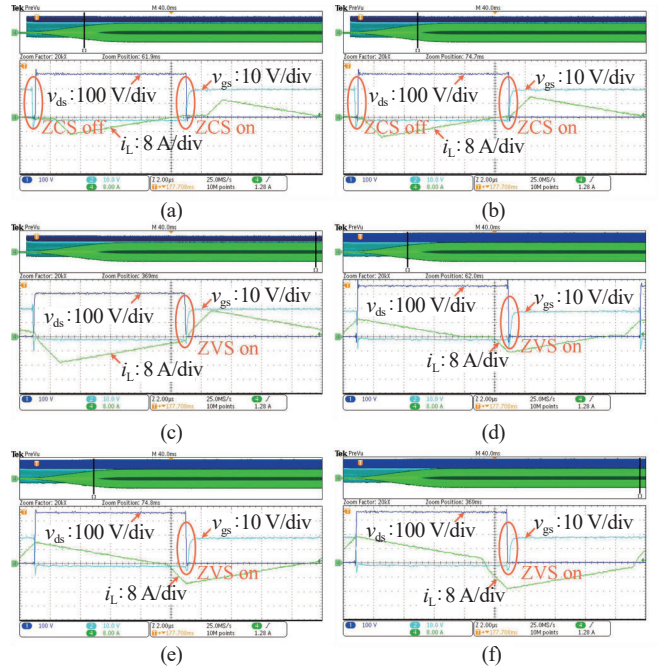


Fig. 19. The switching waveforms with  $V_i = 300$  V,  $V_o = 350$  V. (a)  $S_1$  in Boost\_DCM. (b)  $S_1$  in Boost\_BCM. (c)  $S_1$  in Boost\_CCM. (d)  $S_7$  in Boost\_DCM. (e)  $S_7$  in Boost\_BCM. (f)  $S_7$  in Boost\_CCM.

$S_8$  all behave similarly to  $S_7$ .

Further experiments are conducted with  $V_o$  set to 280 V and 230 V, respectively. The waveforms of Buck\_DCM, Buck\_BCM and Buck\_CCM are presented in Fig. 17, thereby validating the effectiveness of the proposed method across a wide range of output voltage.

### B. The Experiment Under Step-Up Conditions ( $M < 1$ )

With the settings  $V_i = 300$  V,  $V_o = 350$  V, Fig. 18 shows that the converter transitions through Boost\_DCM, Boost\_BCM, and Boost\_CCM, seamlessly. The switching waveforms of  $S_1$  and  $S_7$  are depicted in Fig. 19. In Boost\_DCM and Boost\_

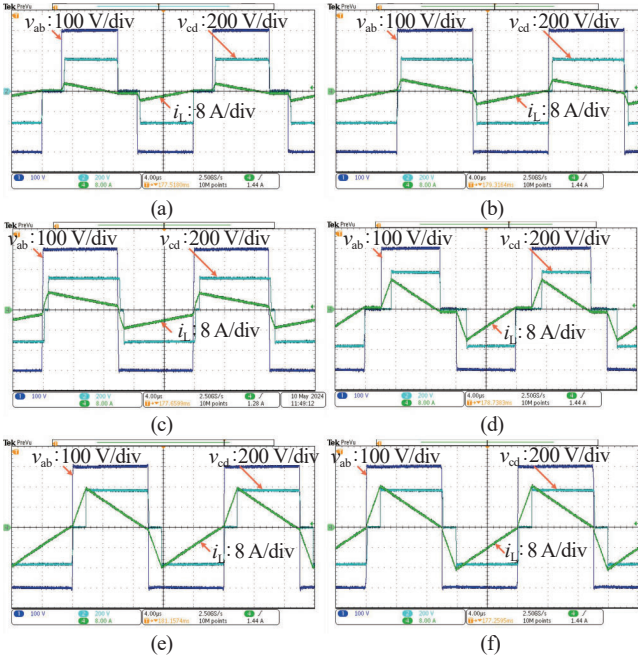


Fig. 20. The waveforms under step-up conditions with  $V_i = 300$  V. (a)  $V_o = 320$  V in Boost\_DCM. (b)  $V_o = 320$  V in Boost\_BCM. (c)  $V_o = 320$  V in Boost\_CCM. (d)  $V_o = 370$  V in Boost\_DCM. (e)  $V_o = 370$  V in Boost\_BCM. (f)  $V_o = 370$  V in Boost\_CCM.

BCM,  $S_1$  achieves ZCS, and in Boost\_CCM, it achieves ZVS.  $S_2 - S_6$  behave similarly to  $S_1$ .  $S_7$  achieves ZVS across all three modes, and  $S_8$  has the same performance as  $S_7$ .

Furthermore, experiments are conducted with  $V_o$  set to 320 V and 370 V, respectively. The waveforms of Boost\_DCM, Boost\_BCM, and Boost\_CCM are displayed in Fig. 20.

### C. Current Stress Analysis

The curves of the current stress by employing the method proposed are illustrated in Fig. 21, and the comparison is made with the optimization methods presented in [21].

As can be observed from Fig. 21(a), under the condition of  $M = 1.67$ , the current stress of the proposed method is significantly lower over the full power range compared to other methods. From Fig. 21(b), it is evident that under the condition of  $M = 0.65$ , the current stress of the proposed method is smaller over the majority of the power range. During the transition from light load to heavy load, the introduction of the high-slope inductor current in the Boost\_CCM mode results in the current stress being slightly higher than that of the TPS-CO within a certain power range. Furthermore, the current stress is obviously decreased under heavy load by the proposed method.

### D. Power Losses and Efficiency Performance

Fig. 22 illustrates the power losses in various components of the experimental prototype operating under Buck\_DCM and Boost\_DCM. The power losses include switching loss, conduction loss, transformer core loss, transformer copper loss, and other loss. The term ‘‘other loss’’ refers to the additional

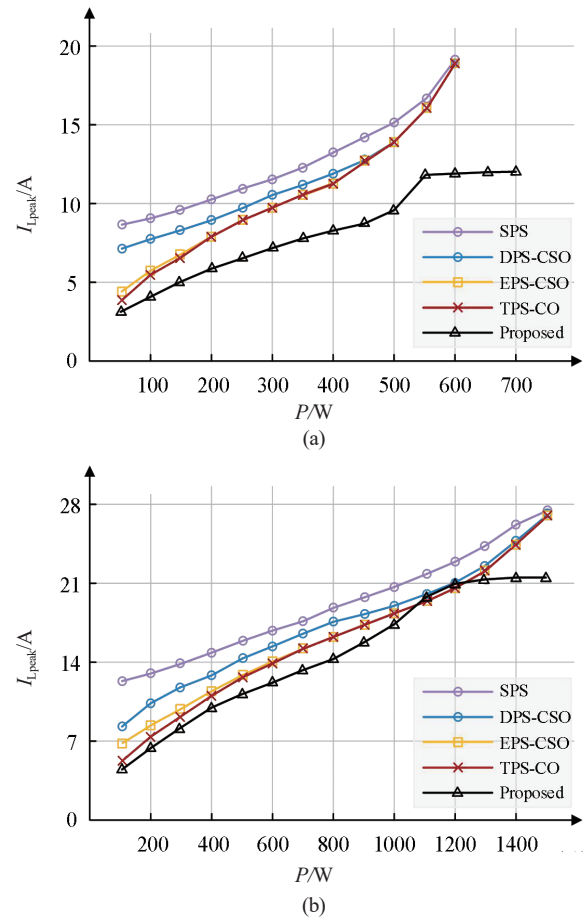


Fig. 21. The curves of the current stress versus transferred power under various control methods. (a) Step-down conditions with  $M = 1.67$ . (b) Step-up conditions with  $M = 0.625$ .

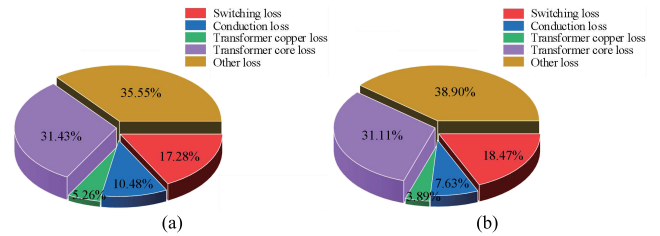


Fig. 22. The power losses of the prototype. (a) Buck\_DCM with  $V_i = 300$  V,  $V_o = 250$  V,  $P = 570$  W. (b) Boost\_DCM with  $V_i = 300$  V,  $V_o = 350$  V,  $P = 620$  W.

loss caused by sampling circuits, snubber circuits and PCB trace resistances, etc.

The curves of the efficiency under step-down and step-up conditions are presented in Fig. 23, which indicates that the prototype exhibits good excellent operational performance, with an overall high efficiency, peaking at 98.6%.

### E. Comparison With Other Methods

A comparison of the proposed method with others is presented in Table IV. As shown in Table IV, while the method in [17] reports the highest efficiency, its performance at higher switching frequencies remains untested. Moreover, its reliance

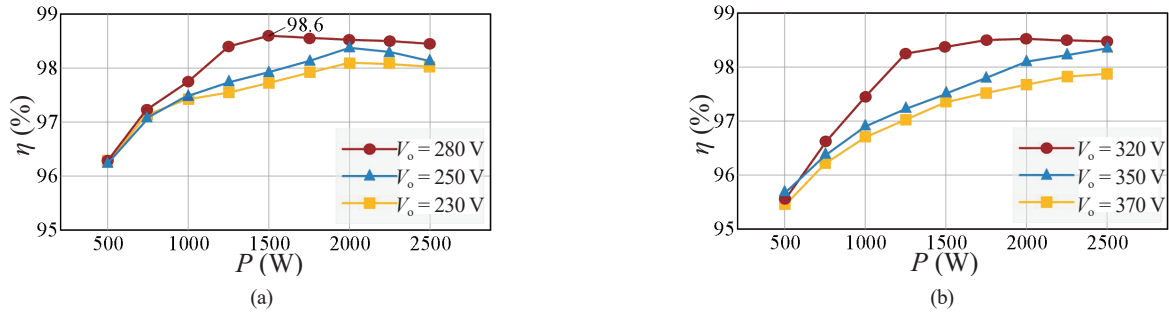


Fig. 23. The curves of the efficiency versus transferred power. (a) Step-down conditions. (b) Step-up conditions.

TABLE IV  
EXPERIMENTAL PARAMETERS

The converter	Input dc voltage/V	Output dc voltage/V	Switching frequency/kHz	Controller complexity	Rated power/kW	Max efficiency/%
[17]	640	250–950	25	High	11	98.8
[19]	200	230, 160	20	Middle	1.3	98.3
[23]	70–110	60	20	Middle	1	97.1
[25]	200–400	300	100	Middle	1.2	95.8
Presented	300	230–370	50	Low	2.5	98.6

on lookup tables poses challenges in real-time application. Both the voltage regulation capability and switching frequency in [19] are limited, with efficiency falling below 96% under heavy-load conditions. The switching frequency and the efficiency are lower in [23]. In [25], although the highest frequency is achieved, the efficiency is compromised, reducing its applicability. Moreover, the latter three methods involve complex and time-consuming analysis of mathematical formulas, resulting in increased control difficulty.

## VI. CONCLUSION

This article proposes a soft-switching control method designed for the DAB converter to operate efficiently across the full power and wide voltage regulation range. Utilizing the principle of voltage superposition, the DAB converter is innovatively transformed into an FSBB converter through the decomposition of the midpoint voltage waveforms  $v_{ab}$  and  $v_{cd}$ . Based on the equivalent circuit, a hybrid phase-shift control method is proposed, which categorizes the DAB converter into six operating modes according to the transferred power, with all six modes facilitating soft-switching of the switching devices. To realize seamless transitions between proposed modes, a unified uni-variate control method is introduced, along with the construction of a closed-loop control system. This method not only simplifies the control process but also facilitates real-time computation, making it compatible with common DSP. The experimental results from the prototype have demonstrated that the proposed method enables the DAB converter to achieve global soft-switching operation over the full power and wide voltage regulation range, resulting in enhanced operational efficiency.

## REFERENCES

- [1] S. S. H. Yazdi, K. Rouzbehi, M. J. Carrizosa, A. Heidary, and M. Bagheri, "Modeling, control, and operation of an M-DAB DC-DC converter for interconnection of HVDC grids," in *IEEE Systems Journal*, vol. 17, no. 2, pp. 2652–2663, Jun. 2023.
- [2] P. F. S. Costa, P. H. B. Löbler, L. Roggia, and L. Schuch, "Modeling and control of DAB converter applied to batteries charging," in *IEEE Transactions on Energy Conversion*, vol. 37, no. 1, pp. 175–184, Mar. 2022.
- [3] S. Chaurasiya and B. Singh, "A bidirectional fast EV charger for wide voltage range using three-level DAB based on current and voltage stress optimization," in *IEEE Transactions on Transportation Electrification*, vol. 9, no. 1, pp. 1330–1340, Mar. 2023.
- [4] N. Hou and Y. W. Li, "Overview and comparison of modulation and control strategies for a nonresonant single-phase dual-active-bridge DC-DC Converter," in *IEEE Transactions on Power Electronics*, vol. 35, no. 3, pp. 3148–3172, Mar. 2020.
- [5] D. Mou, L. Yuan, Q. Luo, Y. Li, C. Liu, J. Zheng, and Z. Zhao, "Overview of multi-degree-of-freedom modulation techniques for dual active bridge converter," in *IEEE Journal of Emerging and Selected Topics in Power Electronics*, vol. 11, no. 6, pp. 5724–5737, Dec. 2023.
- [6] R. W. A. A. De Doncker, D. M. Divan, and M. H. Kheraluwala, "A three-phase soft-switched high-power-density DC/DC converter for high-power applications," in *IEEE Transactions on Industry Applications*, vol. 27, no. 1, pp. 63–73, Jan.-Feb. 1991.
- [7] Q. Gu, L. Yuan, J. Nie, J. Sun, and Z. Zhao, "Current stress minimization of dual-active-bridge DC-DC converter within the whole operating range," in *IEEE Journal of Emerging and Selected Topics in Power Electronics*, vol. 7, no. 1, pp. 129–142, Mar. 2019.
- [8] B. Zhao, Q. Song, W. Liu, and Y. Sun, "Overview of dual-active-bridge isolated bidirectional DC-DC converter for high-frequency-link power-conversion system," in *IEEE Transactions on Power Electronics*, vol. 29, no. 8, pp. 4091–4106, Aug. 2014.
- [9] H. Bai, Z. Nie, and C. C. Mi, "Experimental comparison of traditional phase-shift, dual-phase-shift, and model-based control of isolated bidirectional DC-DC converters," in *IEEE Transactions on Power Electronics*, vol. 25, no. 6, pp. 1444–1449, Jun. 2010.
- [10] F. Krismer and J. W. Kolar, "Efficiency-optimized high-current dual active bridge converter for automotive applications," in *IEEE Transactions on Industrial Electronics*, vol. 59, no. 7, pp. 2745–2760, Jul. 2012.
- [11] B. Zhao, Q. Yu, and W. Sun, "Extended-phase-shift control of isolated bidirectional DC-DC converter for power distribution in microgrid," in

*IEEE Transactions on Power Electronics*, vol. 27, no. 11, pp. 4667–4680, Nov. 2012.

- [12] H. Bai and C. Mi, “Eliminate reactive power and increase system efficiency of isolated bidirectional dual-active-bridge DC-DC converters using novel dual-phase-shift control,” in *IEEE Transactions on Power Electronics*, vol. 23, no. 6, pp. 2905–2914, Nov. 2008.
- [13] P. Wang, X. Chen, C. Tong, P. Jia, and C. Wen, “Large- and small-signal average-value modeling of dual-active-bridge DC-DC converter with triple-phase-shift control,” in *IEEE Transactions on Power Electronics*, vol. 36, no. 8, pp. 9237–9250, Aug. 2021.
- [14] J. Tian, F. Wang, F. Zhuo, Y. Wang, H. Wang, and Y. Li, “A zero-backflow-power EPS control scheme with multiobjective coupled-relationship optimization in DAB-based converter,” in *IEEE Journal of Emerging and Selected Topics in Power Electronics*, vol. 10, no. 4, pp. 4128–4145, Aug. 2022.
- [15] L. Xin, Z. Haoyu, Q. Ya, and S. Junkang, “Current stress optimization of dual active bridge converter based on dual phase shift control,” in *Proceedings of 2020 IEEE 9th Joint ITAIC*, Chongqing, China, 2020, pp. 717–724.
- [16] L. Zhu, A. R. Taylor, G. Liu, and K. Bai, “A multiple-phase-shift control for a SiC-based EV charger to optimize the light-load efficiency, current stress, and power quality,” in *IEEE Journal of Emerging and Selected Topics in Power Electronics*, vol. 6, no. 4, pp. 2262–2272, Dec. 2018.
- [17] D. Lyu, C. Straathof, T. B. Soeiro, Z. Qin, and P. Bauer, “ZVS-optimized constant and variable switching frequency modulation schemes for dual active bridge converters,” in *IEEE Open Journal of Power Electronics*, vol. 4, pp. 801–816, 2023.
- [18] X. Li, X. Zhang, F. Lin, C. Sun, and K. Mao, “Artificial-intelligence-based triple phase shift modulation for dual active bridge converter with minimized current stress,” in *IEEE Journal of Emerging and Selected Topics in Power Electronics*, vol. 11, no. 4, pp. 4430–4441, Aug. 2023.
- [19] A. Tong, L. Hang, G. Li, X. Jiang, and S. Gao, “Modeling and analysis of a dual-active-bridge-isolated bidirectional DC/DC converter to minimize RMS current with whole operating range,” in *IEEE Transactions on Power Electronics*, vol. 33, no. 6, pp. 5302–5316, Jun. 2018.
- [20] N. Hou, W. Song, and M. Wu, “Minimum-current-stress scheme of dual active bridge DC-DC converter with unified phase-shift control,” in *IEEE Transactions on Power Electronics*, vol. 31, no. 12, pp. 8552–8561, Dec. 2016.
- [21] Y. Zhang, J. Zong, F. Zhang, X. Li, Y. Wei, and H. Ma, “A comprehensive optimization strategy of DAB converter with minimal current stress and full soft switching in the whole operating range,” in *IEEE Journal of Emerging and Selected Topics in Power Electronics*, vol. 12, no. 1, pp. 129–142, Feb. 2024.
- [22] Q. Ren and S. Ai, “A three degree freedom optimal control strategy of dual-active-bridge converters for full range operations,” (in Chinese) in *Proceedings of CSEE*, vol. 40, no. 11, pp. 3613–3622, Jun. 2020.
- [23] J. Huang, Y. Wang, Z. Li, and W. Lei, “Unified triple-phase-shift control to minimize current stress and achieve full soft-switching of isolated bidirectional DC-DC converter,” in *IEEE Transactions on Industrial Electronics*, vol. 63, no. 7, pp. 4169–4179, Jul. 2016.
- [24] J. Zhang, D. Sha, and P. Ma, “A dual active bridge DC-DC-based single stage AC-DC converter with seamless mode transition and high power factor,” in *IEEE Transactions on Industrial Electronics*, vol. 69, no. 2, pp. 1411–1421, Feb. 2022.
- [25] Z. Guo, “Modulation scheme of dual active bridge converter for seamless transitions in multiworking modes compromising ZVS and conduction loss,” in *IEEE Transactions on Industrial Electronics*, vol. 67, no. 9, pp. 7399–7409, Sept. 2020.
- [26] F. Krismer and J. W. Kolar, “Closed form solution for minimum conduction loss modulation of DAB converters,” in *IEEE Transactions on Power Electronics*, vol. 27, no. 1, pp. 174–188, Jan. 2012.
- [27] Z. Yu, H. Kapels and K. F. Hoffmann, “High efficiency bidirectional DC-DC converter with wide input and output voltage ranges for battery systems,” in *Proceedings of PCIM Europe*, Nuremberg, Germany, 2015, pp. 1–8.
- [28] B. Zhao, Q. Song, and W. Liu, “Power characterization of isolated bidirectional dual-active-bridge DC-DC converter with dual-phase-shift control,” in *IEEE Transactions on Power Electronics*, vol. 27, no. 9, pp. 4172–4176, Sept. 2012.



**Yuhang Zhang** was born in Hebei, China. He received the B.S. degree from the College of Electrical and Information Engineering, Hunan University, Changsha, China. He is currently working towards the M.S. degree in electrical engineering at Hunan University, Changsha, China. His current research interests include application and control of bidirectional dc-dc converters.



**Yong Li** received the B.Sc. and Ph.D. degrees from the College of Electrical and Information Engineering, Hunan University, Changsha, China, in 2004 and 2011, respectively. He is currently a full Professor of electrical engineering with Hunan University. His current research interests include power system stability analysis and control, ac/dc energy conversion systems and equipment, analysis and control of power quality, and HVDC and FACTS technologies.



**Jianghu Wan** was born in Sichuan, China, in 1991. He received the B.S., M.S. and Ph.D. degrees, in 2014, 2017 and 2024, respectively, from Central South University, Changsha, China. His current research interests include bidirectional dc-dc converters, control of three-phase PWM rectifier, and soft-switching technology.



**Tingkun Weng** received the M.S. degree in 2024 in electrical engineering from Hunan University, Changsha, China. He is currently working at Technical Skills Training Center of State Grid Hunan Electric Power Company (Changsha Electric Power Technical College). His research interests include flux pump, wireless energy transmission and high temperature superconductivity.



**Jie Zhang** was born in Chongqing, China, in 1999. He received B.S. degree from the College of Electrical and Information Engineering, Hunan University, Changsha, China, in 2022. He is currently working the M.S. degree in Hunan University, Changsha, China. His research interests include active power decoupling control and bidirectional dc/dc converters.



**Yijia Cao** was born in Hunan, China, in 1969. He received the graduation degree from Xi’an Jiaotong University, Xi’an, China in 1988, and the M.Sc. and Ph.D. degrees from Huazhong University of Science and Technology (HUST), Wuhan, China, in 1991 and 1994, respectively. From September 1994 to April 2000, he was a Visiting Research Fellow and a Research Fellow with Loughborough University, Loughborough, U.K., Liverpool University, Liverpool, U.K., and the University of the West England, Bristol, U.K. From 2000 to 2001, he was a Professor with HUST, and from 2001 to 2008, he was a Professor with Zhejiang University, Hangzhou, China, and from 2008 to 2018, he was a Professor with Hunan University, Changsha, China. He was appointed as the Vice President of Hunan University in 2008. He is currently a Professor with Changsha University of Science and Technology, Changsha. His research interests include power system stability control and the application of intelligent systems in power systems.